IOP Publishing Phys. Med. Biol. 63 (2018) 045006 (16pp) https://doi.org/10.1088/1361-6560/aaa8a6

Physics in Medicine & Biology

IPEM Institute of Physics and Engineering in Medicine

PAPER

RECEIVED
11 August 2017

REVISED
11 December 2017

ACCEPTED FOR PUBLICATION
18 January 2018

PUBLISHED
12 February 2018

Joint estimation of activity and attenuation for PET using pragmatic MR-based prior: application to clinical TOF PET/MR whole-body data for FDG and non-FDG tracers

Sangtae Ahn[1,5], Lishui Cheng[1], Dattesh D Shanbhag[2], Hua Qian[1], Sandeep S Kaushik[2], Floris P Jansen[3] and Florian Wiesinger[4]

[1] GE Global Research, Niskayuna, NY, United States of America
[2] GE Global Research, Bangalore, India
[3] GE Healthcare, Waukesha, WI, United States of America
[4] GE Healthcare, Munich, Germany
[5] Author to whom any correspondence should be addressed.

E-mail: ahns@ge.com

Keywords: PET/MR, TOF, attenuation correction, joint estimation, MLAA

Supplementary material for this article is available online

Abstract

Accurate and robust attenuation correction remains challenging in hybrid PET/MR particularly for torsos because it is difficult to segment bones, lungs and internal air in MR images. Additionally, MR suffers from susceptibility artifacts when a metallic implant is present. Recently, joint estimation (JE) of activity and attenuation based on PET data, also known as maximum likelihood reconstruction of activity and attenuation, has gained considerable interest because of (1) its promise to address the challenges in MR-based attenuation correction (MRAC), and (2) recent advances in time-of-flight (TOF) technology, which is known to be the key to the success of JE. In this paper, we implement a JE algorithm using an MR-based prior and evaluate the algorithm using whole-body PET/MR patient data, for both FDG and non-FDG tracers, acquired from GE SIGNA PET/MR scanners with TOF capability. The weight of the MR-based prior is spatially modulated, based on MR signal strength, to control the balance between MRAC and JE. Large prior weights are used in strong MR signal regions such as soft tissue and fat (i.e. MR tissue classification with a high degree of certainty) and small weights are used in low MR signal regions (i.e. MR tissue classification with a low degree of certainty). The MR-based prior is pragmatic in the sense that it is convex and does not require training or population statistics while exploiting synergies between MRAC and JE. We demonstrate the JE algorithm has the potential to improve the robustness and accuracy of MRAC by recovering the attenuation of metallic implants, internal air and some bones and by better delineating lung boundaries, not only for FDG but also for more specific non-FDG tracers such as ^{68}Ga-DOTATOC and ^{18}F-Fluoride.

1. Introduction

Simultaneous PET/MR (Vandenberghe and Marsden 2015) is an emerging hybrid imaging modality, which enables simultaneous acquisition of complementary information from PET and MR with simplified workflow and high throughput, providing new opportunities in neurology (Heiss 2016), oncology (Fraum *et al* 2015, Samarin *et al* 2015) and cardiology (Nekolla and Rischpler 2016).

PET provides quantitative information for applications including tumor treatment response monitoring (Wahl *et al* 2009), prognosis (Berghmans *et al* 2008), and brain function study (Tai and Piccini 2004). Attenuation correction is one of the primary data correction steps critical to accurate quantitation. In PET/CT, bi-linear or tri-linear scaling of CT images is a clinical standard for attenuation correction (Kinahan *et al* 2003). In PET/MR, accurate and robust attenuation correction remains challenging because of distinct imaging physics of PET

and MR, and substantial efforts are currently being put into MR-based attenuation correction (MRAC) (Keereman *et al* 2013, Vandenberghe and Marsden 2015).

The most common approach to MRAC is to segment MR images into certain classes such as fat, water, lung and air, and generate an attenuation map by assigning a pre-determined attenuation coefficient to each class (Hofmann *et al* 2009, Martinez-Möller *et al* 2009, Schulz *et al* 2011). MR is well known for its excellent soft tissue contrast but the imaging modality has difficulty in distinguishing between bone and air, which produce similarly low MR signals despite substantially different attenuation coefficients. In addition, magnetic susceptibility effects of metallic implants cause large signal voids in surrounding tissues (Schneck 1996). Therefore, segmentation-based MRAC has challenges in areas such as bone, air and metallic implants. To address the issues, dedicated MRI sequences such as ultrashort echo time (UTE) (Catana *et al* 2010, Keereman *et al* 2010) and zero echo time (ZTE) (Sekine *et al* 2016, Wiesinger *et al* 2016, 2018) that facilitate bone depiction have been investigated. The MRI sequences have successfully been applied to brain imaging and recently shown promise for pelvic imaging (Leynes *et al* 2017). Other approaches to MRAC include atlas-based and template-based methods (Rota Kops and Herzog 2007, Hofmann *et al* 2008, Burgos *et al* 2014). These methods have been successful for brain imaging but less so for whole-body imaging because of considerable anatomical variations in the patient population (Martinez-Möller *et al* 2012, Vandenberghe and Marsden 2015).

An alternative approach is based on joint estimation (JE) of activity and attenuation from PET emission data, which is also known as maximum likelihood reconstruction of activity and attenuation (MLAA) (Nuyts *et al* 1999). JE has a long history in emission tomography (Censor *et al* 1979), and it is well known that a solution to the JE problem is non-unique and typically suffers from cross-talk artifacts due to inextricable effects of activity and attenuation on emission scan data. However, Defrise *et al* (2012) have shown in their milestone paper that the activity image and the attenuation correction factors can be uniquely determined, by emission data only, up to a scaling constant if time of flight (TOF) information is available. This implies TOF information removes cross-talk artifacts in JE solutions, except for scaling, in theory. Because of its applicability to PET/MR and/or recent developments in TOF technologies, JE methods have recently attracted considerable interest (Cheng *et al* 2016a, Li *et al* 2017, Mihlin and Levin 2017). For an extensive overview on the subject of JE the interested reader is referred to the review paper by Berker and Li (2016).

Even if TOF data are available, the scaling constant for JE cannot be determined from emission data only (Defrise *et al* 2012), and cross-talk artifacts still exist in the real world although less severe than those in a non-TOF case (Rezaei *et al* 2012, Boellaard *et al* 2014). Furthermore, JE problems are ill-conditioned and vulnerable to modeling and data correction errors, and statistical noise. To address the issues, various types of prior information have been incorporated into JE. The third quartile (Rezaei *et al* 2012) and the mode (Boellaard *et al* 2014) of attenuation coefficients within the body, and the total activity in the image volume (Rezaei *et al* 2014) and in each image plane (Bal *et al* 2017) are constrained. A multimodal prior for attenuation coefficients is used (Nuyts *et al* 2013). Li *et al* (2015) show that boundary conditions combined with consistency conditions ensure the solution uniqueness. Salomon *et al* (2011) use geometrical information obtained from MR image segmentation to parameterize the attenuation map using piecewise uniform regional basis functions.

In PET/MR attenuation correction, a sensible way of fully exploiting available information will be to (1) rely on MR-based information in regions of high MR signal response (i.e. soft-tissue) and (2) let JE determine the attenuation in uncertain, low MR-signal regions (e.g. implants, bone and air). For example, an uncertain region in MR images, likely to include bone, air cavities, metallic implants and lungs, can be identified by segmenting low MR signal regions (Ahn *et al* 2013, 2015, 2016, Ahn and Manjeshwar 2015, Mehranian and Zaidi 2015b, 2015d, Heußer *et al* 2016, Mehranian *et al* 2016), by using a bone probability map (Mehranian and Zaidi 2015b, 2015d), or by thresholding posterior probabilities (Wang *et al* 2012). Alternatively, the uncertain region can include the following: the outside of the MR field of view (FOV), which is usually smaller than PET FOV, to complete the truncated region (Nuyts *et al* 2013); MR signal voids due to metal susceptibility artifacts to recover implant attenuation (Fuin *et al* 2017); lung regions to address patient-specific and/or spatially-varying lung densities (Berker *et al* 2012, Mehranian and Zaidi 2015c); and the outside of the body to estimate the attenuation of headphones and RF coils (Heußer *et al* 2017). In a PET/CT application, high attenuation coefficient regions in a CT-based attenuation map have been considered as an uncertain region to distinguish between iodine-containing CT contrast agents and bone (Laymon *et al* 2003, Laymon and Bowsher 2013). In the selective JE approach where an uncertain region is identified and the attenuation of the uncertain region is determined by JE, the following priors for the attenuation coefficients of the uncertain region have been used: a multimodal prior (Nuyts *et al* 2013, Mehranian and Zaidi 2015b, 2015d, Heußer *et al* 2016, 2017, Mehranian *et al* 2016), a unimodal prior (Ahn *et al* 2015, 2016, Mehranian and Zaidi 2015c), and a uniform prior (Fuin *et al* 2017). Berker *et al* (2012) have used a regional basis function to represent the uncertain region of the attenuation map as in Salomon *et al* (2011). For the attenuation coefficients outside the uncertain region, unimodal priors (Wang *et al* 2012, Ahn *et al* 2015, 2016, Mehranian and Zaidi 2015b, 2015d, 2016, Heußer *et al* 2016) can be used, or the attenuation coefficients can be fixed as determined based on MR or CT (Laymon *et al* 2003, Berker *et al* 2012, Ahn *et al* 2013, Laymon and

Bowsher 2013, Nuyts *et al* 2013, Mehranian and Zaidi 2015c, Fuin *et al* 2017, Heußer *et al* 2017). Alternatively, Li *et al* (2013) used MR-based joint entropy priors for the attenuation map, and Benoit *et al* (2016) have used UTE and T1-weighted MR images to control the step size of a JE algorithm.

In this paper, we implement a JE algorithm using an MR-based prior, which is unimodal Gaussian based on the MR-segmentation based attenuation map. The prior weight is spatially modulated such that the weight is large in strong MR signal regions, which are likely to consist of soft tissue, and the weight is small in low MR signal regions, whose tissue class is uncertain, and which may include bones, internal air, metallic implants and lungs. The prior weight is further modulated to address remaining JE artifacts such as cross-talk artifacts. The MR-based prior is simple and pragmatic; they are convex, beneficial to numerical optimization, and do not require any training or population statistics.

The JE algorithm with the MR-based prior is demonstrated on whole-body clinical TOF PET/MR data acquired on a clinical PET/MR scanner with TOF capability (Levin *et al* 2016), focusing on challenging regions such as metallic implants, internal air, lungs and bone. Whole-body clinical results are reported here including thoracic, abdomen and pelvic regions whereas JE results in the literature have been shown mostly for specific anatomical regions. In addition to FDG, we also include non-FDG patient data to examine the effects of specific uptake and low background activity of non-FDG tracers on JE results, which have rarely been evaluated for whole-body imaging in the literature.

Some preliminary results have been presented in IEEE Nuclear Science Symposium (NSS) and Medical Imaging Conference (MIC) (Ahn *et al* 2015, Cheng *et al* 2016b) and International Society for Magnetic Resonance in Medicine (ISMRM) Annual Meeting (Ahn *et al* 2016).

2. Methods

2.1. Clinical PET/MR data

Whole-body PET/MR scans were acquired for thirteen patients using GE SIGNA PET/MR scanner (GE Healthcare, Waukesha, WI, USA), whose TOF timing resolution is <400 ps (Levin *et al* 2016). The average patient weight was 78.7 ± 19.2 kg (mean ± standard deviation) and the average body mass index was 25.8 ± 5.2 kg m^{-2}. Patients 1–9 were injected with ^{18}F-FDG, patients 10–12 with ^{68}Ga-DOTATOC (Hofmann *et al* 2001) and patient 13 with ^{18}F-Fluoride tracers (Grant *et al* 2008). The average injected activity was 252.3 ± 66.7 MBq. For MR, a dedicated 3D gradient echo (GRE) scan with Dixon-type fat-water separation was acquired (flip angle 5°, scan time 18 s, FOV 50 × 50 × 31.2 cm^3, and image matrix 256 × 256 × 120 for each bed position) (Wollenweber *et al* 2013a, 2013b). For PET, TOF emission data were acquired with transaxial FOV of 60 cm and axial FOV of 25 cm (for each bed position).

2.2. MR-based attenuation correction (MRAC)

An MR-based attenuation map was generated using 4-class (water, fat, lung and air) segmentation of MR images (Wollenweber *et al* 2013b, Shanbhag *et al* 2015) where N4 bias field correction (Tustison *et al* 2010) was applied to MR images prior to segmentation; and truncation completion was performed using a skin mask derived from an image reconstructed based on TOF data without attenuation correction. Hardware attenuation for table and rigid RF coils with known locations (e.g. brain, head and neck, and posterior body array coils) was obtained from pre-acquired templates; and attenuation for flexible coils was ignored. For the head, an atlas-based method (Wollenweber *et al* 2013a) was used although our focus in this paper is on the body. The MR-based attenuation map was generated using in-house software based on MATLAB (MathWorks, Natick, MA, USA) and ITK (Kitware, Clifton Park, NY, USA), which does not match the scanner-provided attenuation map when signal voids are present, as the scanner algorithm performs certain post-processing steps to detect and correct for voids. Our goal here is not to optimize MRAC and reduce artifacts occurring in MR data processing; instead, we choose to preserve such artifacts in order to examine how our JE algorithm works in their presence.

2.3. JE algorithm using MR-based prior

2.3.1. Uncertain MR-region segmentation

Uncertain regions with low MR signals, likely to include bone, air, lungs and metallic implants, were segmented in bias-corrected MR images using ITK and MATLAB. In lung and abdomen regions, a vertebra region was first identified (Shanbhag *et al* 2015). In the vertebra region, the multi Otsu method was applied to the in-phase MR image with four levels (Liao *et al* 2001) and two darkest classes (with weak MR signals) were considered as uncertain regions. In the non-vertebra region, multi-step thresholding and region growing were used as follows. Huang's fuzzy thresholding method (Huang and Wang 1995) and Otsu's method (Otsu 1979) were applied to the in-phase MR image for binary image segmentation. Segmented lung and air regions obtained from MRAC (section 2.2) were used as seed points for 2D region growing on the binary mask from Huang's thresholding method and then the updated regions were used as seed points for 3D region growing on the binary mask from

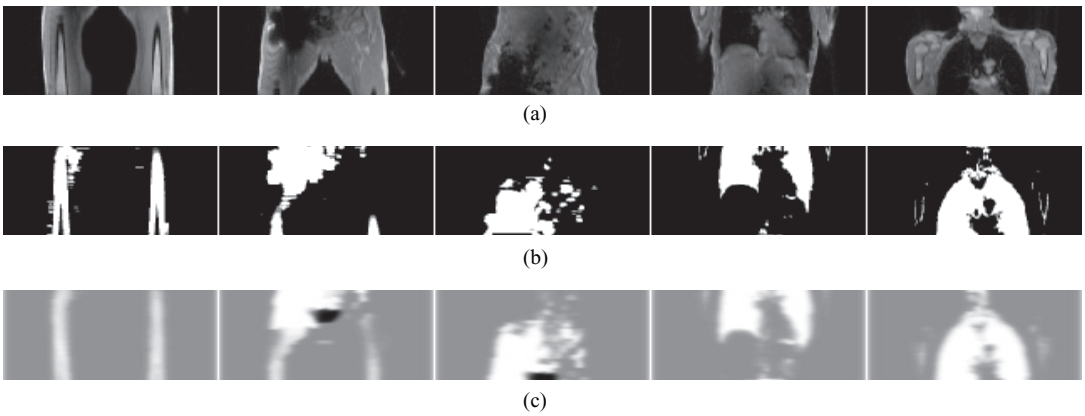

Figure 1. Example coronal slices of (a) in-phase MR image, (b) uncertain regions (represented by white regions), and (c) MR-based prior weight map where the range is between 0.002 (white) and 2 (black).

Otsu's method to obtain uncertain regions in the non-vertebra regions. In pelvic regions, a histogram based thresholding was applied to the in-phase MR image to obtain uncertain regions and small isolated components in the uncertain regions were collated together. Figure 1(b) shows example uncertain regions.

2.3.2. *MR-based prior*

We use the following regularization function for the attenuation map μ:

$$R(\mu) = \beta^{\mathrm{MR}} \sum_j w_j^{\mathrm{MR}} \frac{\left(\mu_j - \mu_j^{\mathrm{MR}}\right)^2}{2} + \frac{\beta^{\mathrm{smooth}}}{2} \sum_j \sum_{k \in \mathcal{N}_j} w_{jk}^{\mathrm{smooth}} \frac{\left(\mu_j - \mu_k\right)^2}{2}$$

where the first term on the right-hand is the MR-based prior and the second term is the conventional roughness penalty that encourages image smoothness by penalizing differences between neighboring voxels. Here μ^{MR} denotes the MR-based attenuation map (section 2.2), μ_j and μ_j^{MR} represent the attenuation coefficient of the jth voxel for μ and μ^{MR}, respectively, β^{MR} and β^{smooth} are parameters that control the global strength of the MR-based prior and the roughness penalty, respectively, w_j^{MR} are prior weights that control the local strength of the MR-based prior, $\mathcal{N}_j$ denotes a set of voxels that are adjacent to voxel j, and w_{jk}^{smooth} are typically chosen from $1, 1/\sqrt{2}$ and $1/\sqrt{3}$ depending on the distance between voxels j and k. In this paper, $\beta^{\mathrm{MR}} = 5 \times 10^5$ and $\beta^{\mathrm{smooth}} = 2 \times 10^4$ were empirically chosen.

A small prior weight (e.g. $w_j^{\mathrm{MR}} = 2 \times 10^{-3}$) was used in the uncertain regions (section 2.3.1), and a large prior weight (e.g. $w_j^{\mathrm{MR}} = 1$) was used outside the uncertain regions. The prior weights were further modulated, motivated by empirical observations, as follows. We often observe overestimated attenuation coefficients near the skin, particularly in arms, in JE reconstructed attenuation maps (e.g. figure 3(c), and figures S1(c), S3(c), S6(c) and S7(c) (stacks.iop.org/PMB/63/045006/mmedia) of supplementary data). The reason for the artifacts is believed to be that lines of response (LORs) passing through the regions near the body boundary do not have enough activity and attenuation projections and therefore those regions are sensitive to noise and modeling errors. To reduce such artifacts, regions close to the body boundary (e.g. <35 mm) were excluded from the uncertain regions. In addition, sometimes, we would still observe cross-talk artifacts in JE reconstructed attenuation maps even with TOF data for high activity regions such as heart (e.g. figure 5(c)) and bladder (e.g. figure 2(c), and figure S9(c) of supplementary data). From an activity image reconstructed with 1 iteration of TOF OSEM with MRAC, which by default is calculated as part of JE iterations (section 2.3.3), we segmented a sizeable high activity region (e.g. such that its activity exceeds five times the mean activity and its volume is >50 cm^3), and then assigned a large prior weight (e.g. $w_j^{\mathrm{MR}} = 2$) to the high activity region. The MR-based prior weight map was filtered with 2 cm full-width at half-maximum (FWHM) Gaussian in-plane filter and a three-point axial filter [1, 2, 1]/4. Figure 1(c) shows example prior weight maps.

2.3.3. *Update of activity and attenuation*

The activity image λ and the attenuation map μ were alternatively updated as in MLAA (Nuyts *et al* 1999). The MR-based attenuation map (section 2.2) was used as the initial attenuation map $\mu^{(0)}$ and a uniform image was used as the initial activity image $\lambda^{(0)}$.

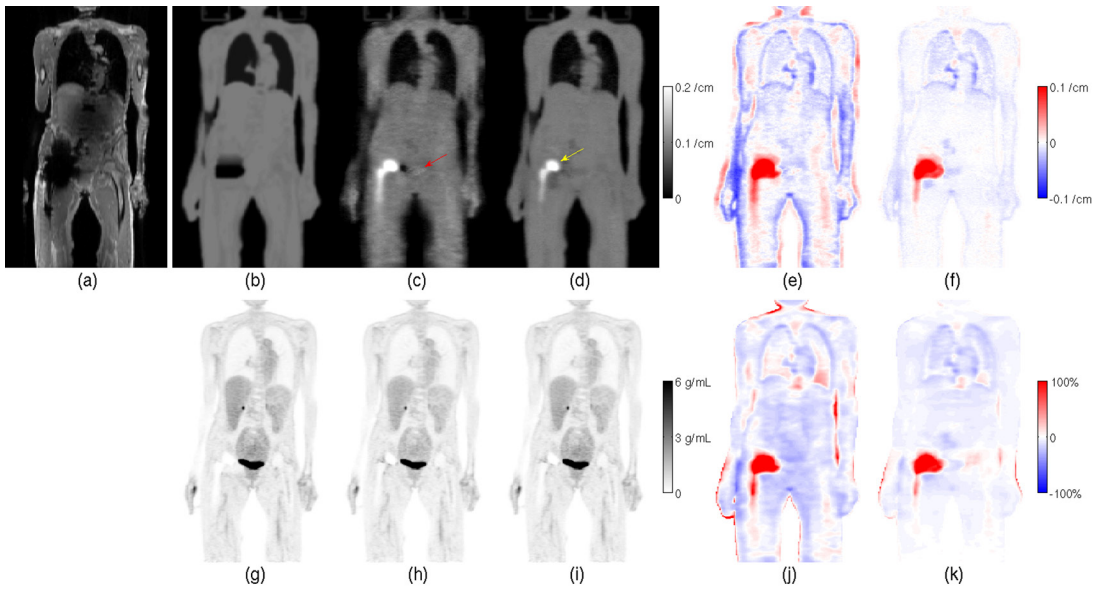

Figure 2. Example coronal slice containing a hip endoprosthesis, for patient 1 with ^{18}F-FDG, of (a) in-phase MR image; attenuation maps (b) μ^{MR} based on MR, (c) μ^{JEnoMR} based on JE without MR-based priors, and (d) μ^{JE} based on JE with MR-based priors; differences in the attenuation maps, (e) $\mu^{\mathrm{JEnoMR}} - \mu^{\mathrm{MR}}$, and (f) $\mu^{\mathrm{JE}} - \mu^{\mathrm{MR}}$; TOF OSEM reconstructed activity images (g) λ^{MR} based on μ^{MR}, (h) $\lambda^{\mathrm{JEnoMR}}$ based on μ^{JEnoMR}, and (i) λ^{JE} based on μ^{JE}; and relative differences in the TOF OSEM reconstructed images, (j) $(\lambda^{\mathrm{JEnoMR}} - \lambda^{\mathrm{MR}})/\lambda^{\mathrm{MR}}$, and (k) $(\lambda^{\mathrm{JE}} - \lambda^{\mathrm{MR}})/\lambda^{\mathrm{MR}}$. The yellow arrow indicates the recovered metallic implant in the JE reconstructed attenuation map in (d), and the red arrow indicates the overestimated attenuation region corresponding to the bladder in μ^{JEnoMR}.

For the kth iteration (for $k = 1, 2, \ldots$), the kth iterate $\lambda^{(k)}$ of the activity image was calculated updating the previous iterate $\lambda^{(k-1)}$ by TOF OSEM (Hudson and Larkin 1994) with 1 iteration and 28 subsets where attenuation correction was based on the previous iterate $\mu^{(k-1)}$ of the attenuation map:

$$\lambda_j^{(k,m)} = \frac{\lambda_j^{(k,m-1)}}{\sum_{i\in S_m}\sum_t a_{ij}^t c_i\left(\mu^{(k-1)}\right)} \sum_{i\in S_m}\sum_t \frac{a_{ij}^t c_i\left(\mu^{(k-1)}\right) y_i^t}{\sum_{j'} a_{ij'}^t c_i\left(\mu^{(k-1)}\right)\lambda_{j'}^{(k,m-1)} + r_i^t}$$

for $m = 1, \ldots, M$ with $\lambda_j^{(k,0)} = \lambda_j^{(k-1)}$ and $\lambda_j^{(k)} = \lambda_j^{(k,M)}$ where a_{ij}^t represent the probability that a photon pair emitted from voxel j is detected and recorded for LOR i and TOF bin t in the absence of attenuation, y_i^t are measured PET data, r_i^t denote estimated background events including scatters and randoms, S_m represents the mth subset of LORs, M is the number of subsets (e.g. $M = 28$), and c_i are attenuation factors expressed by $c_i(\mu) = \exp(-\sum_j l_{ij}\mu_j)$ with l_{ij} being the length of the intersection between LOR i and voxel j. Here a_{ij}^t includes normalization factors as well as geometric forward projection.

The kth iterate $\mu^{(k)}$ of the attenuation map was calculated using ordered subsets transmission (OSTR) (Erdoğan and Fessler 1999a, Ahn *et al* 2012) with 5 iterations and 28 subsets where the regularization function $R(\mu)$ as described in section 2.3.2 was used:

$$\mu_j^{(k,m)} = \mathrm{median}\left\{0,\ U,\ \mu_j^{(k,m-1)} + \frac{1}{d_j}\left\{M\sum_{i\in S_m} l_{ij} b_i\left(\lambda^{(k)}\right) c_i\left(\mu^{(k,m-1)}\right)\left(1 - \frac{y_i}{b_i\left(\lambda^{(k)}\right) c_i\left(\mu^{(k,m-1)}\right) + r_i}\right) - \frac{\partial R\left(\mu^{(k,m-1)}\right)}{\partial \mu_j}\right\}\right\}$$

with $\mu_j^{(k,0)} = \mu_j^{(k-1)}$ and $\mu_j^{(k)} = \mu_j^{(k,M)}$ where $y_i = \sum_t y_i^t$, $r_i = \sum_t r_i^t$, $b_i(\lambda) = \sum_j a_{ij}\lambda_j$ with $a_{ij} = \sum_t a_{ij}^t$, $\mathrm{median}\{\cdot\}$ is the median of a given set, $U > 0$ is the upper bound imposed on attenuation coefficients, for which we used 1 cm^{-1} (we have not observed any case where the upper bound constraint becomes active), and

$$d_j = \max\left\{\sum_{i:y_i>r_i,y_i>0} l_{ij}\sum_{j'} l_{ij'}\frac{(y_i - r_i)^2}{y_i} + \beta^{\mathrm{MR}} w_j^{\mathrm{MR}} + 2\beta^{\mathrm{smooth}}\sum_{k\in\mathcal{N}_j} w_{jk}^{\mathrm{smooth}}, \epsilon\right\}$$

with a small constant $\epsilon > 0$, for which we used 10^{-12}. Note $\mathrm{median}\{0, U, x\}$ for $x \in \mathbb{R}$ is equivalent to the projection of x onto the closed interval $[0, U]$. A derivation of the update equation above is given in appendix. We also show the relationship between OSTR and maximum likelihood for transmission tomography (MLTR) used in MLAA (Rezaei *et al* 2012) in the appendix. Since d_j is constant in λ and μ, it can be precomputed for a given data set and does not need to be recomputed. The ϵ term prevents d_j from being zero. Usually, the regularization term, $\beta^{\mathrm{MR}} w_j^{\mathrm{MR}} + 2\beta^{\mathrm{smooth}}\sum_{k\in\mathcal{N}_j} w_{jk}^{\mathrm{smooth}}$, keeps d_j well away from being too small. Even in an unregularized case

$(\beta^{\mathrm{MR}} w_j^{\mathrm{MR}} + 2\beta^{\mathrm{smooth}} \sum_{k\in\mathcal{N}_j} w_{jk}^{\mathrm{smooth}} = 0)$ with low counts ($y_i = 0$) and/or high scatter and random fractions ($r_i > y_i$), although d_j can be as small as ϵ, imposing the constraint $0 \leqslant \mu_j \leqslant U$ by the median operator prevents the iterates $\mu_j^{(k,m)}$ from diverging.

In this paper, we used 5 outer iterations, each of which consists of 1 iteration of TOF OSEM with 28 subsets, and 5 iterations of OSTR with 28 subsets. The activity image was initialized with a uniform image only for the first outer iteration. After JE iterations, a final activity image was reconstructed using 2 iterations of TOF OSEM with 28 subsets where attenuation correction was based on the JE reconstructed attenuation map, and point spread functions in sinogram space (Alessio *et al* 2010) were used; the reconstructed activity image was post-filtered with 6.4 mm FWHM Gaussian in-plane filter and a three-point axial filter [1, 4, 1]/6.

To examine the impact of TOF information on JE results, in addition to the JE algorithm using TOF data as described above, we ran a non-TOF version of JE where TOF OSEM was replaced with non-TOF OSEM when updating the activity image in JE iterations and reconstructing the final activity image, and then compared the results from TOF and non-TOF JE. When non-TOF OSEM was used, the final activity image was post-filtered with 4.0 mm FWHM Gaussian in-plane filter and a three-point axial filter [1, 6, 1]/8. Because TOF information accelerates convergence (Surti and Karp 2015), TOF OSEM images are usually noisier than non-TOF OSEM images with the same number of iterations. Therefore, we applied heavier filtering to TOF OSEM images than to non-TOF OSEM images, to make the image noise levels more comparable.

To study the impact of scatter estimation on JE results (Laymon *et al* 2006), we compared JE results for the cases where scatters were re-estimated every outer iteration and where scatters estimated based on the initial MR-based attenuation map were used throughout JE iterations. Here we used a model-based method for scatter estimation (Watson 2000, Qian *et al* 2010).

3. Results

Figures 2–7 (and figures S1–S11 of supplementary data) show example coronal slices of in-phase MR image; MR-based attenuation map μ^{MR} (section 2.2); JE reconstructed attenuation maps, μ^{JEnoMR} with no MR-based prior (i.e. $\beta^{\mathrm{MR}} = 0$ yet $\beta^{\mathrm{smooth}} = 2 \times 10^4$ as in section 2.3.2), and μ^{JE} with the MR-based prior ($\beta^{\mathrm{MR}} = 5 \times 10^5$ and $\beta^{\mathrm{smooth}} = 2 \times 10^4$ as in section 2.3.2); and TOF OSEM reconstructed activity images, λ^{MR} with attenuation correction based on the MR-based attenuation map μ^{MR}, $\lambda^{\mathrm{JEnoMR}}$ based on μ^{JEnoMR}, and λ^{JE} based on μ^{JE}. To better visualize the differences between the attenuation maps and between the activity images, the figures also show the difference between the JE reconstructed attenuation maps and the MR-based attenuation map, $\mu^{\mathrm{JEnoMR}} - \mu^{\mathrm{MR}}$ and $\mu^{\mathrm{JE}} - \mu^{\mathrm{MR}}$; and the relative difference between the activity images reconstructed based on the MR-based attenuation map and the JE reconstructed attenuation maps, $(\lambda^{\mathrm{JEnoMR}} - \lambda^{\mathrm{MR}})/\lambda^{\mathrm{MR}}$ and $(\lambda^{\mathrm{JE}} - \lambda^{\mathrm{MR}})/\lambda^{\mathrm{MR}}$. The JE reconstructed attenuation maps were calculated bed-wise, and the bed-wise attenuation maps for each patient were stitched to form a whole-body attenuation map as shown in the figures. When the relative difference of the activity images was calculated, the activity images were filtered using a $3 \times 3 \times 3$ moving average filter before calculating the difference. Note JE with no MR-based prior (μ^{JEnoMR} and $\lambda^{\mathrm{JEnoMR}}$ with $\beta^{\mathrm{MR}} = 0$) is similar to MLAA (Nuyts *et al* 1999).

Patient 1 had a hip endoprosthesis and pedicle screws. JE algorithms recovered the attenuation of the metal implants (figures 2(c), (d) and 3(c), (d)). The metal implants produced susceptibility artifacts, that is, signal voids in MR (figures 2(a) and 3(a)), which in turn resulted in misclassification as internal air in the MR-based attenuation maps (figures 2(b) and 3(b)).

Lung boundaries in JE reconstructed attenuation maps (figures 2(c) and (d)) for patient 1, when compared to the MR image (figure 2(a)), appear more accurately delineated than those in the MR-based attenuation map (figure 2(b)). Better lung delineation of JE can also be observed in figures S1, S6, S7, S9 and S11 of supplementary data (for patients 2, 8, 9, 12 and 13, respectively). The results imply JE algorithms can correct for lung segmentation errors, if exist, in MRAC.

In figures 4–7 (for patients 4, 6, 11 and 13, respectively), the JE reconstructed attenuation maps (figures 4(c), 5(c), 6(c) and 7(c), 4(d), 5(d), 6(d) and 7(d)) show better recovery of internal air in abdomen regions than the MR-based attenuation maps (figures 4(b), 5(b), 6(b) and 7(b)) (see MR in-phase images in figures 4(a), 5(a), 6(a) and 7(a)). JE's better recovery of abdominal internal air can also be seen in figures S4 (for patient 7), S5 and S6 (for patient 8), S8 (for patient 10), and S9 and S10 (for patient 12) of supplementary data (see also figures S21 and S22, compared to figures S6 and S8, respectively, of supplementary data); some internal air is still missing in JE reconstructed attenuation maps, though (figures 7 and S9). The results imply JE algorithms can better recover abdominal internal air than MRAC when MR image segmentation of internal air fails.

In general, bone attenuation was not well recovered by the JE algorithms. However, some leg bones were recovered in JE reconstructed attenuation maps (figures 4 and 5 for patients 4 and 6; and figures S1, S2 and S11, of supplementary data, for patients 2, 3 and 13).

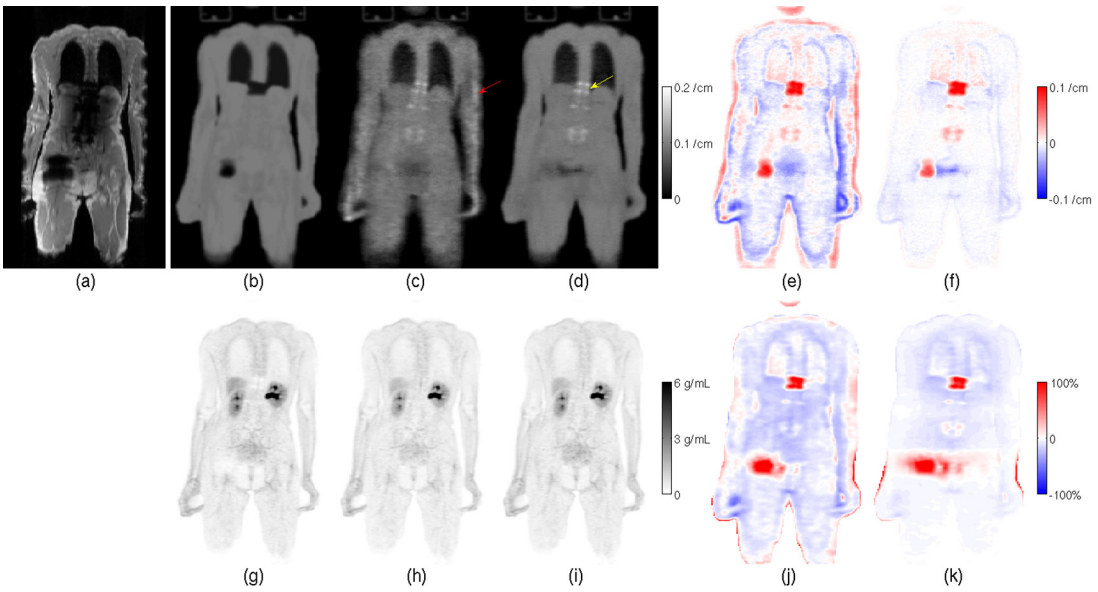

Figure 3. Example coronal slice containing pedicle screws, for patient 1 with ^{18}F-FDG, of (a) in-phase MR image; attenuation maps (b) μ^{MR} based on MR, (c) μ^{JEnoMR} based on JE without MR-based priors, and (d) μ^{JE} based on JE with MR-based priors; differences in the attenuation maps, (e) $\mu^{\mathrm{JEnoMR}} - \mu^{\mathrm{MR}}$, and (f) $\mu^{\mathrm{JE}} - \mu^{\mathrm{MR}}$; TOF OSEM reconstructed activity images (g) λ^{MR} based on μ^{MR}, (h) $\lambda^{\mathrm{JEnoMR}}$ based on μ^{JEnoMR}, and (i) λ^{JE} based on μ^{JE}; and relative differences in the TOF OSEM reconstructed images, (j) $(\lambda^{\mathrm{JEnoMR}} - \lambda^{\mathrm{MR}})/\lambda^{\mathrm{MR}}$, and (k) $(\lambda^{\mathrm{JE}} - \lambda^{\mathrm{MR}})/\lambda^{\mathrm{MR}}$. The yellow arrow indicates recovered metal implants in the JE reconstructed attenuation map in (d), and the red arrow indicates the overestimated attenuation region close to the arm boundary in μ^{JEnoMR}.

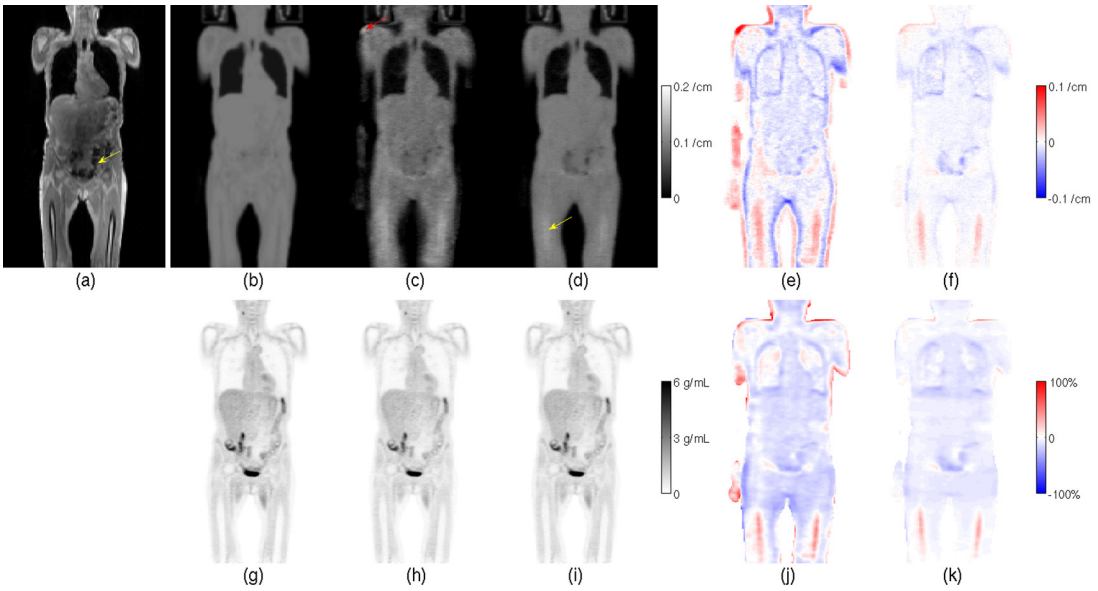

Figure 4. Example coronal slice, for patient 4 with ^{18}F-FDG, of (a) in-phase MR image; attenuation maps (b) μ^{MR} based on MR, (c) μ^{JEnoMR} based on JE without MR-based priors, and (d) μ^{JE} based on JE with MR-based priors; differences in the attenuation maps, (e) $\mu^{\mathrm{JEnoMR}} - \mu^{\mathrm{MR}}$, and (f) $\mu^{\mathrm{JE}} - \mu^{\mathrm{MR}}$; TOF OSEM reconstructed activity images (g) λ^{MR} based on μ^{MR}, (h) $\lambda^{\mathrm{JEnoMR}}$ based on μ^{JEnoMR}, and (i) λ^{JE} based on μ^{JE}; and relative differences in the TOF OSEM reconstructed images, (j) $(\lambda^{\mathrm{JEnoMR}} - \lambda^{\mathrm{MR}})/\lambda^{\mathrm{MR}}$, and (k) $(\lambda^{\mathrm{JE}} - \lambda^{\mathrm{MR}})/\lambda^{\mathrm{MR}}$. The yellow arrows indicates abdominal internal air in the MR image (a) and leg bone in the JE reconstructed attenuation map in (d), and the red arrow indicates the overestimated attenuation region close to the body boundary in μ^{JEnoMR}.

Overall, attenuation maps reconstructed by the JE algorithm without MR-based priors in figures 2–5(c) and 7(c), and figures S1–S11(c) of supplementary data, were noisier than those reconstructed by the JE algorithm with the MR-based prior in figures 2–5(d) and 7(d), and figures S1–S11(d) of supplementary data. In addition, the attenuation coefficients in background soft tissue regions of the JE reconstructed attenuation maps without MR-based priors were, by and large, smaller than those of the MR-based attenuation maps (see figures 2–5(e) and 7(e), and figures S1–S11(e) of supplementary data). Given that the MR-based attenuation maps are reasonably accurate in the soft tissue regions, the difference between the MR-based attenuation maps and the JE reconstructed attenuation maps in the background is ascribed to the non-unique scaling of a JE solution. Using the

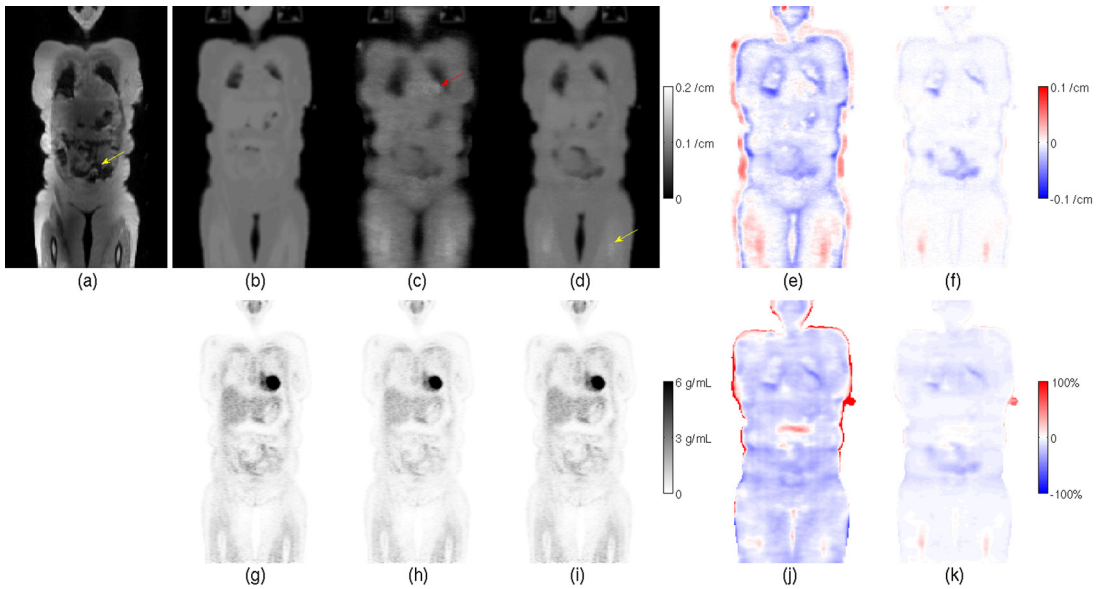

Figure 5. Example coronal slice, for patient 6 with ^{18}F-FDG, of (a) in-phase MR image; attenuation maps (b) μ^{MR} based on MR, (c) μ^{JEnoMR} based on JE without MR-based priors, and (d) μ^{JE} based on JE with MR-based priors; differences in the attenuation maps, (e) $\mu^{JEnoMR} - \mu^{MR}$, and (f) $\mu^{JE} - \mu^{MR}$; TOF OSEM reconstructed activity images (g) λ^{MR} based on μ^{MR}, (h) λ^{JEnoMR} based on μ^{JEnoMR}, and (i) λ^{JE} based on μ^{JE}; and relative differences in the TOF OSEM reconstructed images, (j) $(\lambda^{JEnoMR} - \lambda^{MR})/\lambda^{MR}$, and (k) $(\lambda^{JE} - \lambda^{MR})/\lambda^{MR}$. The yellow arrows indicate abdominal internal air in the MR image (a) and leg bone in the JE reconstructed attenuation map in (d), and the red arrow indicates the overestimated attenuation region corresponding to the heart in μ^{JEnoMR}.

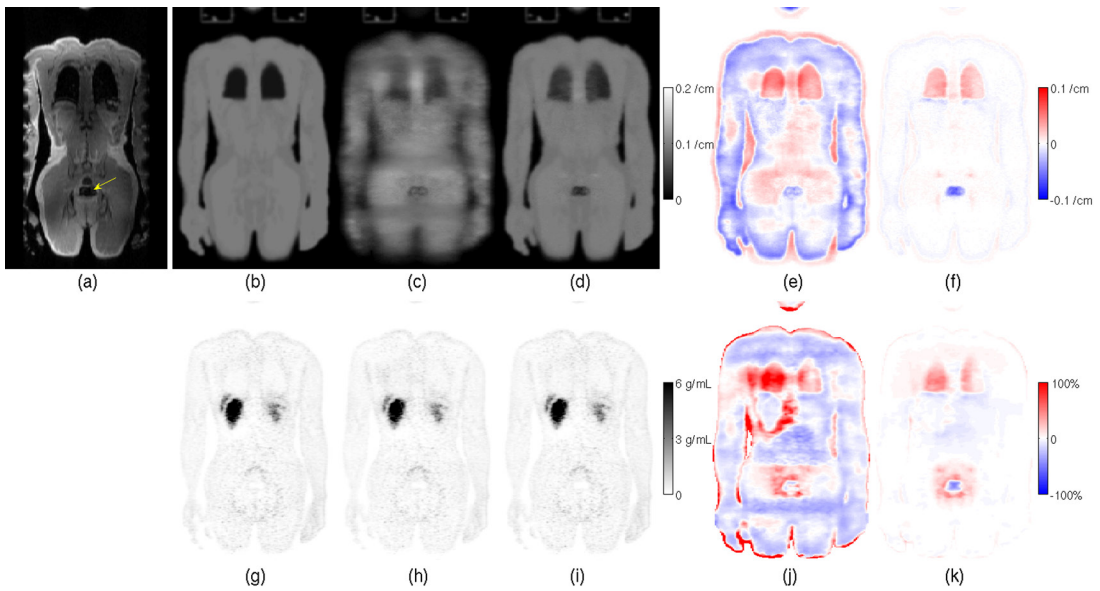

Figure 6. Example coronal slice, for patient 11 with ^{68}Ga-DOTATOC, of (a) in-phase MR image; attenuation maps (b) μ^{MR} based on MR, (c) μ^{JEnoMR} based on JE without MR-based priors, and (d) μ^{JE} based on JE with MR-based priors; differences in the attenuation maps, (e) $\mu^{JEnoMR} - \mu^{MR}$, and (f) $\mu^{JE} - \mu^{MR}$; TOF OSEM reconstructed activity images (g) λ^{MR} based on μ^{MR}, (h) λ^{JEnoMR} based on μ^{JEnoMR}, and (i) λ^{JE} based on μ^{JE}; and relative differences in the TOF OSEM reconstructed images, (j) $(\lambda^{JEnoMR} - \lambda^{MR})/\lambda^{MR}$, and (k) $(\lambda^{JE} - \lambda^{MR})/\lambda^{MR}$. The yellow arrow indicates internal air in the MR image (a).

MR-based prior for JE reduced the difference between the MR-based attenuation maps and the JE reconstructed attenuation maps in the background soft tissue regions (see figures 2–5(f) and 7(f), and figures S1–S11(f) of supplementary data).

In the JE reconstructed attenuation maps without MR-based priors, overestimated attenuation coefficients were observed in hot activity regions such as heart (e.g. see figure 5(c)) and bladder (e.g. see figure 2(c), and figure S9(c) of supplementary data). Such cross-talk artifacts were substantially reduced in the JE reconstructed attenuation maps with the MR-based prior (e.g. see figures 2(d) and 5(d), and figure S9(d) of supplementary data). In addition, overestimated attenuation coefficients were also observed in regions close to

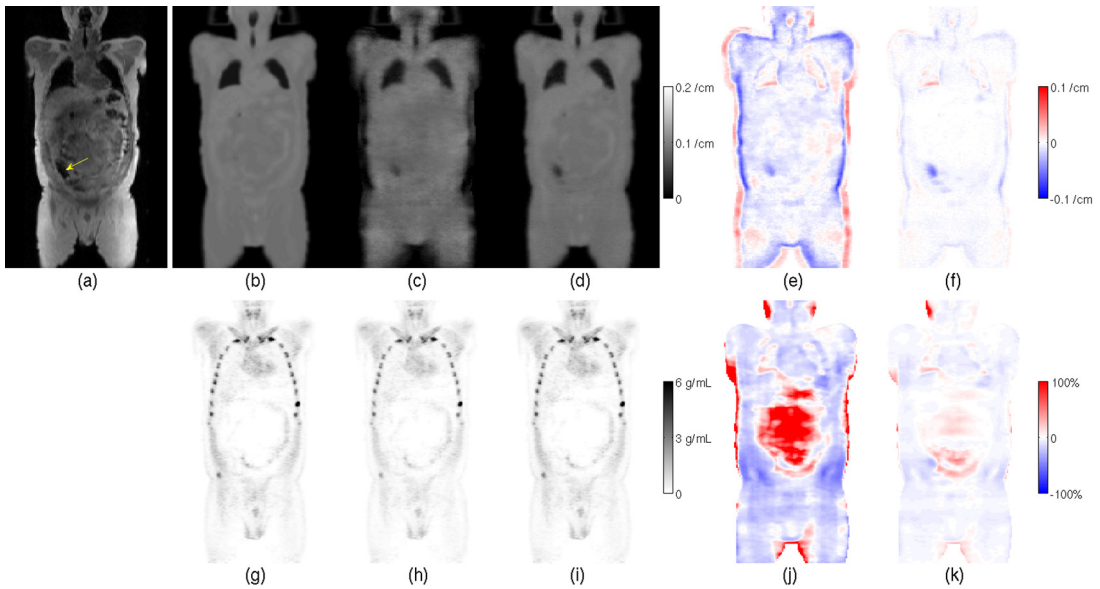

Figure 7. Example coronal slice, for patient 13 with ^{18}F-Fluorine, of (a) in-phase MR image; attenuation maps (b) μ^{MR} based on MR, (c) μ^{JEnoMR} based on JE without MR priors, and (d) μ^{JE} based on JE with MR priors; differences in the attenuation maps, (e) $\mu^{JEnoMR} - \mu^{MR}$, and (f) $\mu^{JE} - \mu^{MR}$; TOF OSEM reconstructed activity images (g) λ^{MR} based on μ^{MR}, (h) λ^{JEnoMR} based on μ^{JEnoMR}, and (i) λ^{JE} based on μ^{JE}; and relative differences in the TOF OSEM reconstructed images, (j) $(\lambda^{JEnoMR} - \lambda^{MR})/\lambda^{MR}$, and (k) $(\lambda^{JE} - \lambda^{MR})/\lambda^{MR}$. The yellow arrow indicates internal air in the MR image (a).

the body boundary such as arms (figure 3(c), and figures S1(c), S3(c), S6(c) and S7(c) of supplementary data) and shoulders (figure 4(c), and figure S5(c) of supplementary data) of the JE reconstructed attenuation maps without MR-based priors. This is believed to be because the regions close to the skin boundary are sensitive to modeling errors and statistical noise. The JE algorithm with the MR-based prior reduced the artifacts by weighting MRAC in those regions (figures 3(d) and 4(d), and figures S1(d), S3(d), S5(d), S6(d) and S7(d) of supplementary data).

Figure 8 shows the impact of TOF information through an example coronal slice for patient 10 scanned with ^{68}Ga-DOTATOC. Internal air adjacent to the bladder (see figure S22 of supplementary data), which is missing in the MR-based attenuation map (figure 8(b)), is recovered in the attenuation map reconstructed by JE using the MR-based prior and TOF data (figure 8(d)) whereas it is not well recovered by JE using non-TOF data (figure 8(c)). In the activity images (figures 8(e) and (f)) reconstructed by non-TOF OSEM based on the MR-based attenuation map (figure 8(b)) and the non-TOF JE reconstructed attenuation map (figure 8(c)), respectively, it can be observed that the activity of the bladder in adjacent coronal slices was spilled over to the internal air region, which was misclassified as soft tissue in the attenuation maps. Figure 8(g), TOF OSEM reconstruction with MRAC (figure 8(b)), shows TOF data reduced the spill-over although not completely. Figure 8(h) shows the JE algorithm using TOF data with the MR-based prior substantially reduced the spill-over artifact. TOF information was also found to help the JE algorithm better recover (compared to JE with non-TOF data) metal implants (figure S12), internal air (figures S14–S20) and leg bones (figures S13 and S15).

We compared the JE reconstructed attenuation maps with the MR-based prior using the following scatter estimation approaches: (1) using fixed scatter estimates based on MRAC throughout JE iterations and (2) re-estimating scatters every JE outer iteration. For patients 2–13, the voxel-wise difference in JE estimated attenuation coefficients for those cases (with and without scatter re-estimation) was smaller than 0.0012 cm^{-1}. For patient 1 having metallic implants, the difference was up to 0.005 cm^{-1}. Figure 9 shows a comparison of fixing scatter estimates (figure 9(a)) and re-calculating scatter estimates (figure 9(b)) for patient 1. The difference in JE reconstructed attenuation maps occurs mostly around the hip implant (figure 9(c)), and scatter re-estimation produced less blurred implant recovery.

4. Discussion

We implemented a JE algorithm using a pragmatic MR-based prior, which is convex and does not require training or population statistics, with a prior weight spatially modulated to synergistically combine MR and TOF PET based JE. One of the contributions of this paper is that the JE algorithm was demonstrated on clinical PET/MR data, acquired by a simultaneous PET/MR scanner with TOF capability, focusing on the body (the results for heads not shown in this paper) whereas JE algorithms in the literature were evaluated mostly on phantom data

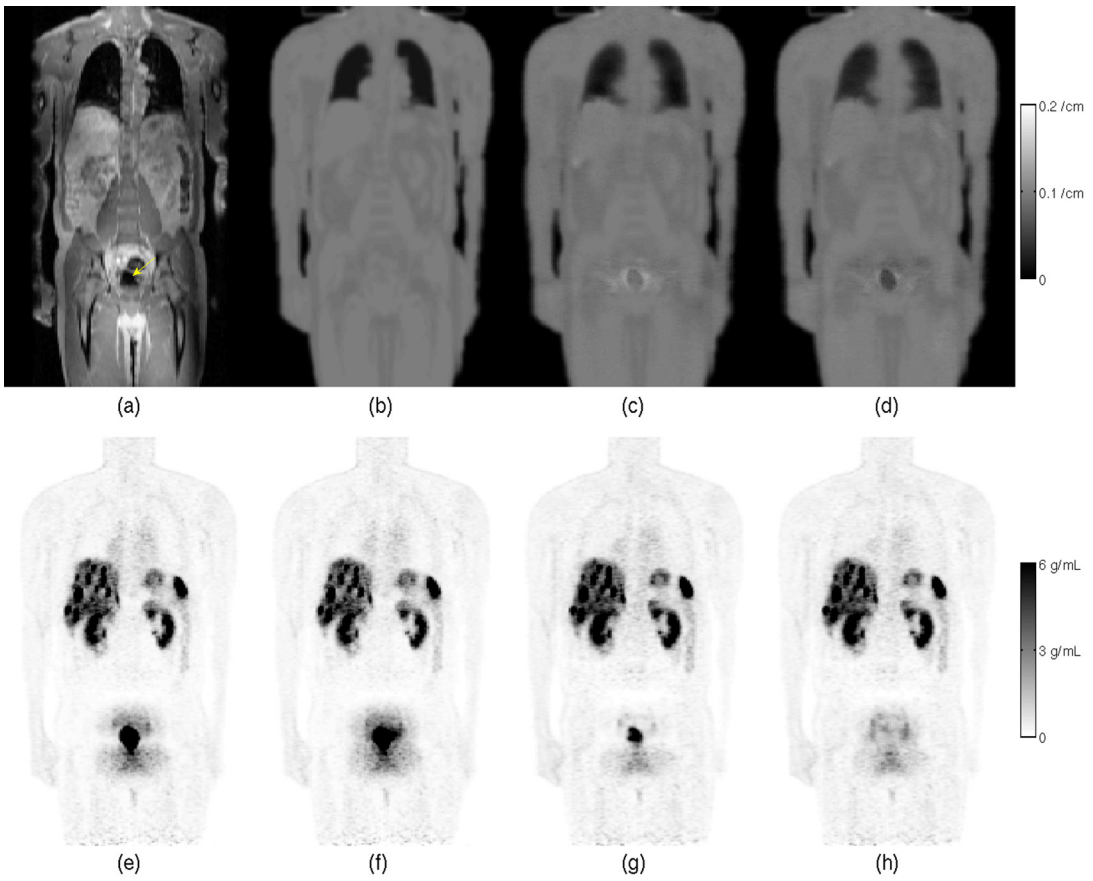

Figure 8. Example coronal slice, for patient 10 with ^{68}Ga-DOTATOC, of (a) in-phase MR image; attenuation maps (b) μ^{MR} based on MR, (c) $\mu^{JEnonTOF}$ based on JE with MR-based priors and non-TOF data, and (d) μ^{JE} based on JE with MR-based priors and TOF data; non-TOF OSEM reconstructed images (e) $\lambda^{MRnonTOF}$ based on μ^{MR} and (f) $\lambda^{JEnonTOF}$ based on $\mu^{JEnonTOF}$; and TOF OSEM reconstructed images (g) λ^{MR} based on μ^{MR} and (h) λ^{JE} based on μ^{JE}. The yellow arrow indicates internal air in the MR image (a) (see also figure S22 of supplementary data).

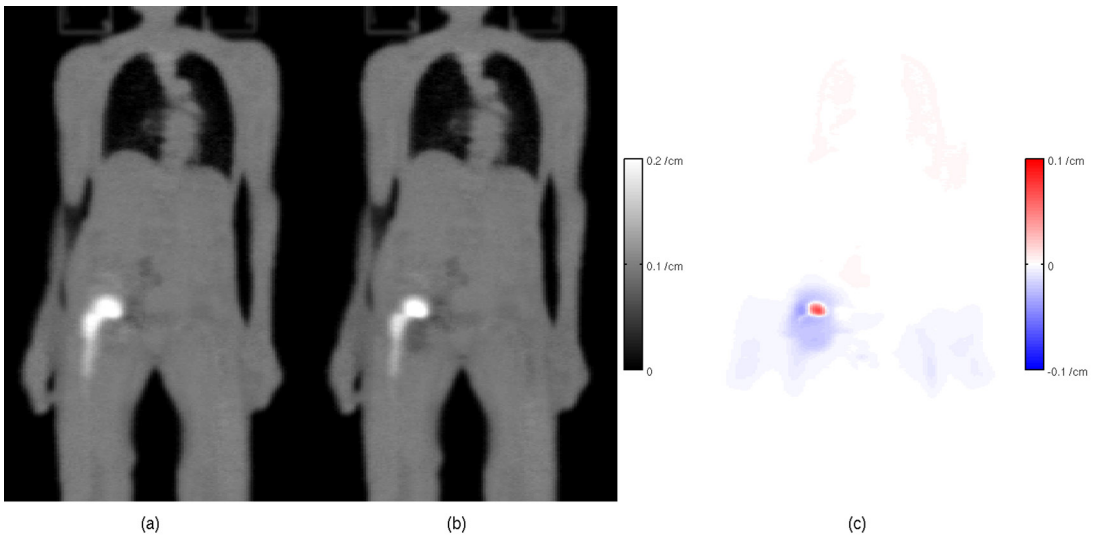

Figure 9. Coronal slice containing the hip endoprosthesis for patient 1 of JE reconstructed attenuation maps with (a) using fixed scatter estimates based on the MR-based attenuation map (figure 2(b)) and (b) with re-estimating scatters every JE outer iteration, and (c) the difference of the attenuation maps (a) and (b).

or specific anatomic regions. In addition to FDG scans, we also demonstrated JE on non-FDG data with more specific uptake patterns and lower background activity.

We observed different types of artifacts in attenuation maps reconstructed by a JE algorithm without MR-based priors, which is similar to MLAA (Nuyts *et al* 1999), in section 3. First, the attenuation coefficients in

soft tissue regions were generally underestimated when compared to MR-based attenuation maps, which are expected to be reasonably accurate in the soft tissue regions. This seems due to the non-uniqueness of a JE solution (Defrise *et al* 2012) (note TOF information does not help resolve the non-unique scaling issue even in an ideal case). The bias in the estimated attenuation coefficients for soft tissue regions could be reduced if the attenuation map μ^{JEnoMR} is scaled such that the third quartile (Rezaei *et al* 2012) or the mode (Boellaard *et al* 2014) of the attenuation coefficients within the body or the mean of the attenuation coefficients in a segmented soft tissue region matches a pre-determined attenuation coefficient of soft tissue. However, because scaling the entire attenuation map is not optimal (Bal *et al* 2017), and furthermore, our purpose was a comparison to JE with no or minimal prior information, we did not scale the attenuation map μ^{JEnoMR} in this study. Note using the MR-based prior does such scaling implicitly. Second, overestimated attenuation coefficients were observed near the body boundary, e.g. in arms and shoulders. Such artifacts have also been observed in Rezaei *et al* (2012) and are thought to be partly due to the non-uniqueness of a JE solution and partly because LORs passing through the regions close to the skin boundary do not have sufficient activity and attenuation projection (Boellaard *et al* 2014) and the regions become sensitive to modeling errors and statistical noise, which are inevitable in a real world. Third, cross-talk artifacts still existed with TOF data (Rezaei *et al* 2012, Boellaard *et al* 2014) and appeared as overestimated attenuation coefficients in hot activity regions such as hearts (Rezaei *et al* 2012) and bladders. Note that the cross-talk artifacts appearing in hot (or cold) activity regions are expected to decrease with better TOF timing resolution (e.g. see figure 3 of Rezaei *et al* (2012) and figure 2 of Boellaard *et al* (2014)). By using the MR-based prior with appropriately modulated prior weights (section 2.3.2), those types of artifacts were substantially reduced.

We observed the JE algorithm with the MR-based prior recover metallic implants and internal air, and delineate lung and tissue boundaries reasonably well. A few remarks are as follows. First, implant management (Schramm *et al* 2014, Fuin *et al* 2017) is a unique application of JE in the sense that PET data provide information about the attenuation of implants and surrounding activity while MR fails to do so. It will be worthwhile to carry out a dedicated, systematic study to focus on the quantitative performance of JE for recovering implant attenuation using multiple patients with metallic implants (note the known attenuation coefficients of implants can be used for evaluation or as prior information). Second, it is an important yet still open question whether JE algorithms can estimate patient-specific and spatially-varying lung attenuation coefficients accurately, besides lung delineation (Rezaei *et al* 2012). Mehranian and Zaidi (2015c) have reported promising initial results on this front. Third, our JE algorithm using the convex, unimodal MR-based prior did not recover bones well except for some large leg and pelvic bones. Mehranian and Zaidi (2015b, 2015d) and Mehranian *et al* (2016) could recover bone attenuation reasonably well in head and neck, and thoracic regions by using a nonconvex multimodal prior based on the population statistics in combination with a bone probability map; extensive clinical evaluation on whether this approach can be applied to whole body in a robust way would be an interesting study.

In the literature, JE algorithms have been evaluated on clinical data with non-FDG tracers such as ^{18}F-FCH (Mehranian and Zaidi 2015d), ^{18}F-FET (Benoit *et al* 2016, Mehranian *et al* 2016) and 11C-PiB (Benoit *et al* 2016) for brain imaging, and ^{18}F-Choline for lung imaging (Mehranian and Zaidi 2015c). However, JE algorithms have rarely been applied to non-FDG whole-body clinical data. In this study, we applied the JE algorithm with the MR-based prior to ^{68}Ga-DOTATOC and ^{18}F-Fluoride whole-body clinical PET/MR data and observed the JE algorithm recover internal air reasonable well, although not completely, for the non-FDG tracers with specific and low background uptake.

A limitation of this study is the lack of quantitative evaluation against a ground truth reference such as CT-based attenuation correction. There are challenges, though, in using CT-based attenuation maps as the ground truth particularly for whole-body imaging because of respiratory motion and the motion of internal organs and air occurring between CT and PET/MR scans. CT scan data for the patients used in this study were unavailable; however, from the clinical PET/MR data, we could still learn a lot about and obtain useful insights into the performance and limitation of the JE algorithms.

In this paper, the regularization parameters were empirically chosen but they worked reasonably well for different patients and tracers. Figure S23 of supplementary data illustrates the impact of the regularization parameters on JE results. As the smoothing parameter β^{smooth} was reduced from 2×10^4 (figure S23(a)) to 2×10^3 (figure S23(b)), the reconstructed attenuation map became noisy particularly in the uncertain regions (e.g. lungs and implant regions) with small w_j^{MR}. On the other hand, when β^{smooth} was increased to 2×10^5 (figure S23(c)), the attenuation map became overly blurred. That is, β^{smooth} controls the image roughness. When the MR-based prior strength parameter β^{MR} was decreased to 10^3, the reconstructed attenuation map (figure S23(e)) became similar to the attenuation map reconstructed by JE without MR-based priors (see figure 2(c)). In contrast, when β^{MR} was increased to 10^6, the attenuation map approached the MR-based attenuation map (figure S23(d)). That is, β^{MR} controls the balance between MRAC and JE (with no prior). Quantitative and systematic tuning of the regularization parameters requires further investigation.

It is well-known that TOF information makes PET quantitation robust to errors in attenuation correction (Conti 2011, Ahn *et al* 2014, Davison *et al* 2015, Mehranian and Zaidi 2015a, ter Voert *et al* 2017) and reduces cross-talk artifacts in JE (Defrise *et al* 2012, Rezaei *et al* 2012, Boellaard *et al* 2014). In this paper, we demonstrated TOF information helps improve JE in recovering attenuation of implants, internal air and bones, resulting in more accurate PET quantitation (e.g. figure 8). There have been a few recent studies to investigate non-TOF JE methods (Benoit *et al* 2016, Heußer *et al* 2016). In addition, Heußer *et al* (2017) and Fuin *et al* (2017) attempted to estimate the attenuation of non-patient hardware (headphone and RF coil) and metallic implants, respectively, using non-TOF PET data. These studies present promising results particularly for a case when TOF data is unavailable. If TOF data are available, the results are expected to improve (Defrise *et al* 2012, Rezaei *et al* 2012, Boellaard *et al* 2014); and as TOF technology further advances (Surti and Karp 2015, Vandenberghe *et al* 2016), the benefit for JE from TOF information will increase accordingly.

We observed, for patient 1 with metal implants, re-estimating scatters for every JE outer iteration results in less blurred implant recovery than using scatter estimates derived based on MRAC. However, for the other patients where the MR-based attenuation map is not as different from the JE reconstructed attenuation map as in patient 1, the difference in JE results made by scatter re-estimation was not that significant (voxel-wise difference $<0.0012\,\mathrm{cm}^{-1}$). There is a trade-off between computation cost and accuracy. It will be sufficient to re-estimate scatters only few times (e.g. once after the final JE iteration) for normal patients without metal implants.

As described in section 2.2, attenuation for tables and rigid RF coils was addressed based on pre-acquired templates, and flexible RF coils were ignored in attenuation correction. Heußer *et al* (2017) showed promising results from using MLAA for recovering attenuation of headphones and RF coils; however, these results are not as satisfactory as those from applying MLAA to patient bodies with implants. In fact, it is more challenging to estimate the attenuation of RF coils by MLAA than to reconstruct that of metallic implants because many of LORs passing through RF coils (outside the patient) have zero activity projection whereas most of LORs passing through implants (inside the patient) have non-zero activity projection even if both RF coils and implants have no uptake of activity. Attenuation correction for flexible RF coils was outside the scope of this paper but the task is worth efforts for future investigation.

We focused on JE of the activity image and the attenuation map, that is, MLAA, in this paper. There is another approach of JE of the activity image and the attenuation correction factors, also known as maximum likelihood reconstruction of activity and attenuation correction factors (MLACF) (Rezaei *et al* 2014) and its simultaneous version sMLACF (Salvo and Defrise 2017). The advantage of the MLACF approach when compared to the MLAA approach is that the computation can be simpler and that normalization factors can also be estimated as being combined with the attenuation correction factors. However, the number of parameters to estimate in the MLACF approach is much larger than that in the MLAA approach for fully 3D imaging, and it is not straightforward how to incorporate prior information about the attenuation map in the image space into the MLACF approach. In addition, when a pseudo (or substitute) CT image is required, e.g. as in MRI-only radiation therapy (Edmund and Nyholm 2017), additional transmission tomographic reconstruction of the attenuation map from the estimated attenuation correction factors is required. Such a trade-off between MLAA and MLACF approaches should be kept in mind when choosing between them.

5. Conclusion

The JE algorithm using the MR-based prior with spatially modulated prior weights to exploit synergies between MRAC and JE was shown to recover metallic implants and internal air and delineate the lung boundary in reconstructed attenuation maps reasonably well for both FDG and non-FDG tracers, addressing the challenges of MRAC. Future work includes quantitative analysis based on tri-modality PET/MR and CT (or PET/CT) scan data, extension to other MRI sequences such as ZTE, and further optimization of parameters.

Acknowledgments

S Ahn, D D Shanbhag, S S Kaushik, F P Jansen and F Wiesinger are employees of General Electric. L Cheng and H Qian were employees of General Electric. The authors thank Ravindra Manjeshwar (formerly, GE Global Research) for his guidance and suggestions in this study, Gaspar Delso, Timothy Deller, Michel Tohme, Jianhua Yu and Yiqiang Jian (GE Healthcare) for help with acquiring and processing the data, and Peter Edic (GE Global Research) for constructive suggestions about the manuscript.

Appendix

We provide a brief derivation of the OSTR update equation given in section 2.3.3. A cost function sought to minimize over $0 \leqslant \mu_j \leqslant U$ is

$$\Phi(\mu) = -L(\mu) + R^{\mathrm{MR}}(\mu) + R^{\mathrm{smooth}}(\mu)$$

where $-L$ is the negative log-likelihood function based on independent Poisson noise models, given by

$$-L(\mu) = \sum_i h_i\left(\sum_j l_{ij}\mu_j\right)$$

with

$$h_i(l) = \sum_i b_i(\lambda)\exp(-l) + r_i - y_i \log\{b_i(\lambda)\exp(-l) + r_i\},$$

and the regularization functions R^{MR} and R^{smooth} are, as described in section 2.3.2, given by

$$R^{\mathrm{MR}}(\mu) = \beta^{\mathrm{MR}} \sum_j w_j^{\mathrm{MR}} \frac{\left(\mu_j - \mu_j^{\mathrm{MR}}\right)^2}{2}$$

$$R^{\mathrm{smooth}}(\mu) = \frac{\beta^{\mathrm{smooth}}}{2} \sum_j \sum_{k\in\mathcal{N}_j} w_{jk}^{\mathrm{smooth}} \frac{(\mu_j - \mu_k)^2}{2}.$$

An approximate version of a separable paraboloidal surrogate for $-L$ at a current iterate $\widehat{\mu}$ with the precomputed curvature (Erdoğan and Fessler 1999a) is

$$Q(\mu;\widehat{\mu}) = \sum_j \left\{ \frac{d_j^*}{2}(\mu_j - \widehat{\mu}_j)^2 - \frac{\partial L(\widehat{\mu})}{\partial \mu_j}(\mu_j - \widehat{\mu}_j) \right\} - L(\widehat{\mu})$$

where d_j^* is given by equation (23) of Erdoğan and Fessler (1999a) as

$$d_j^* = \sum_{i:y_i>r_i,\ y_i>0} l_{ij} \sum_{j'} l_{ij'} \frac{(y_i - r_i)^2}{y_i}.$$

(A function f is said to be separable if it can be written as $f(\mu) = \sum_j f_j(\mu_j)$.) If $y_i = 0$ or $r_i \geqslant y_i$ then $h_i(l)$ is convex according to Lemma 1 of Erdoğan and Fessler (1999b). In this case, a linear function tangent to $h_i(l)$ is a minorizing surrogate function for $h_i(l)$ according to section 3.2 of Hunter and Lange (2012) and the second derivative of the linear surrogate function is zero. The is the reason that the terms in d_j^* for $y_i = 0$ or $r_i \geqslant y_i$ are missing. Because R^{MR} is a separable quadratic function, it can be a separable paraboloidal surrogate for itself:

$$S^{\mathrm{MR}}(\mu;\widehat{\mu}) = \sum_j \left\{ \frac{\beta^{\mathrm{MR}} w_j^{\mathrm{MR}}}{2}(\mu_j - \widehat{\mu}_j)^2 + \frac{\partial R^{\mathrm{MR}}(\widehat{\mu})}{\partial \mu_j}(\mu_j - \widehat{\mu}_j) \right\} + R^{\mathrm{MR}}(\widehat{\mu}) = R^{\mathrm{MR}}(\mu).$$

A separable paraboloidal surrogate for the non-separable quadratic function R^{smooth} is given by

$$S^{\mathrm{smooth}}(\mu;\widehat{\mu}) = \sum_j \left\{ \frac{2\beta^{\mathrm{smooth}} \sum_{k\in\mathcal{N}_j} w_{jk}^{\mathrm{smooth}}}{2}(\mu_j - \widehat{\mu}_j)^2 + \frac{\partial R^{\mathrm{smooth}}(\widehat{\mu})}{\partial \mu_j}(\mu_j - \widehat{\mu}_j) \right\} + R^{\mathrm{smooth}}(\widehat{\mu})$$

(see equations (10) and (14) of Erdoğan and Fessler (1999a)). The factor 2 in the numerator of the first term on the right hand side results from deriving the separable surrogate function S^{smooth} for the non-separable function R^{smooth} (see equations (9) and (10) of Erdoğan and Fessler (1999a)). In contrast, the factor 2 does not appear in S^{MR} because R^{MR} is separable. Now

$$\widetilde{\phi}(\mu;\widehat{\mu}) = Q(\mu;\widehat{\mu}) + S^{\mathrm{MR}}(\mu;\widehat{\mu}) + S^{\mathrm{smooth}}(\mu;\widehat{\mu}) = \sum_j \frac{\widetilde{d}_j}{2}(\mu_j - \widehat{\mu}_j)^2 + \nabla\Phi(\widehat{\mu})(\mu - \widehat{\mu}) + \Phi(\widehat{\mu})$$

is a proper separable surrogate function where

$$\widetilde{d}_j = d_j^* + \beta^{\mathrm{MR}} w_j^{\mathrm{MR}} + 2\beta^{\mathrm{smooth}} \sum_{k\in\mathcal{N}_j} w_{jk}^{\mathrm{smooth}}.$$

To prevent $\widetilde{d}_j$ from being zero or too small, we consider the following surrogate function, which is also a proper separable surrogate function for the cost function $\Phi(\mu)$ at the current iterate $\widehat{\mu}$:

$$\phi(\mu;\widehat{\mu}) = \sum_j \frac{d_j}{2}\left(\mu_j - \widehat{\mu}_j\right)^2 + \nabla\Phi(\widehat{\mu})(\mu - \widehat{\mu}) + \Phi(\widehat{\mu})$$

where $d_j = \max\{\widetilde{d}_j, \epsilon\}$. The next iterate is obtained minimizing the surrogate function ϕ over $0 \leqslant \mu_j \leqslant U$:

$$\mu_j^{\text{next}} = \text{median}\left\{0, U, \widehat{\mu}_j - \frac{1}{d_j}\left\{-\frac{\partial L(\widehat{\mu})}{\partial \mu_j} + \frac{\partial R^{\text{MR}}(\widehat{\mu})}{\partial \mu_j} + \frac{\partial R^{\text{smooth}}(\widehat{\mu})}{\partial \mu_j}\right\}\right\}.$$

When $-\partial L/\partial \mu_j$ is approximated using a subset of the data y_i, the update equation above becomes the OSTR update equation in section 2.3.3 (see equation (24) of Erdoğan and Fessler (1999a)).

When

$$\sum_{j'} -\left.\frac{\partial^2 L(\widehat{\mu})}{\partial \mu_j \partial \mu_{j'}}\right|_{y_i = b_i(\lambda)\exp\left(-\sum_k l_{ik}\widehat{\mu}_k\right) + r_i} = \sum_i l_{ij}\frac{b_i^2(\lambda)\exp\left(-2\sum_k l_{ik}\widehat{\mu}_k\right)}{b_i(\lambda)\exp\left(-\sum_k l_{ik}\widehat{\mu}_k\right) + r_i}\sum_{j'} l_{ij'}$$

is used for d_j^*, the OSTR update equation above becomes the MLTR update equation (see equation (6) of Rezaei *et al* (2012)) if the median operator and the regularization functions are ignored. If

$$y_i \approx b_i(\lambda)\exp\left(-\sum_k l_{ik}\,\widehat{\mu}_k\right) + r_i,$$

which holds approximately after some iterations, then the OSTR and the MLTR update equations become equivalent.

References

Ahn S, Cheng L and Manjeshwar R M 2014 Analysis of the effects of errors in attenuation maps on PET quantitation in TOF PET *Proc. IEEE Nuclear Science Symp. Medical Imaging Conf.*

Ahn S, Cheng L, Shanbhag D and Wiesinger F 2016 Robust PET attenuation correction for PET/MR using joint estimation with MR-based priors: application to whole-body clinical TOF PET/MR data *Proc. Int. Society for Magnetic Resonance in Medicine (ISMRM) Annual Meeting*

Ahn S, Cheng L, Shanbhag D, Wiesinger F and Manjeshwar R 2015 Joint reconstruction of activity and attenuation using MR-based priors: application to clinical TOF PET/MR *Proc. IEEE Nuclear Science Symp. Medical Imaging Conf.*

Ahn S and Manjeshwar R M 2015 Joint estimation of attenuation and activity information using emission data *US Patent Application Publication US* 2015/0065854A1

Ahn S, Qian H and Manjeshwar R M 2012 Convergent iterative algorithms for joint reconstruction of activity and attenuation from time-of-flight PET data *Proc. IEEE Nuclear Science Symp. Medical Imaging Conf.* pp 3695–700

Ahn S, Shanbhag D, Qian H, Kaushik S, Thiruvenkadam S and Manjeshwar R 2013 Improved attenuation correction in PET/MRI by combining MR image segmentation and joint estimation approaches *J. Nucl. Med.* **54** 150 (suppl. 2)

Alessio A M, Stearns C W, Tong S, Ross S G, Kohlmyer S, Ganin A and Kinahan P E 2010 Application and evaluation of a measured spatially variant system model for PET image reconstruction *IEEE Trans. Med. Imaging* **29** 938–49

Bal H, Panin V Y, Platsch G, Defrise M, Hayden C, Hutton C, Serrano B, Paulmier B and Casey M E 2017 Evaluation of MLACF based calculated attenuation brain PET imaging for FDG patient studies *Phys. Med. Biol.* **62** 2542–58

Benoit D, Ladefoged C N, Rezaei A, Keller S H, Andersen F L, Højgaard L, Hansen A E, Holm S and Nuyts J 2016 Optimized MLAA for quantitative non-TOF PET/MR of the brain *Phys. Med. Biol.* **61** 8854–74

Berghmans T *et al* 2008 Primary tumor standardized uptake value (SUVmax) measured on fluorodeoxyglucose positron emission tomography (FDG-PET) is of prognostic value for survival in non-small cell lung cancer (NSCLC): a systematic review and meta-analysis (MA) by the European Lung Cancer Working Party for the IASLC Lung Cancer Staging Project *J. Thorac. Oncol.* **3** 6–12

Berker Y and Li Y 2016 Attenuation correction in emission tomography using the emission data—a review *Med. Phys.* **43** 807–32

Berker Y, Salomon A, Kiessling F and Schulz V 2012 Lung attenuation coefficient estimation using maximum likelihood reconstruction of attenuation and activity for PET/MR attenuation correction *Proc. IEEE Nuclear Science Symp. Medical Imaging Conf.* pp 2282–4

Boellaard R, Hofman M B M, Hoekstra O S and Lammertsma A A 2014 Accurate PET/MR quantification using time of flight MLAA image reconstruction *Mol. Imaging Biol.* **16** 469–77

Burgos N *et al* 2014 Attenuation correction synthesis for hybrid PET-MR scanners: application to brain studies *IEEE Trans. Med. Imaging* **33** 2332–41

Catana C, van der Kouwe A, Benner T, Michel C J, Hamm M, Fenchel M, Fischl B, Rosen B, Schmand M and Sorensen A G 2010 Toward implementing an MRI-based PET attenuation-correction method for neurologic studies on the MR-PET brain prototype *J. Nucl. Med.* **51** 1431–8

Censor Y, Gustafson D E, Lent A and Tuy H 1979 A new approach to the emission computerized tomography problem: simultaneous calculation of attenuation and activity coefficients *IEEE Trans. Nucl. Sci.* **26** 2775–9

Cheng J C K, Salomon A, Yaqub M and Boellaard R 2016a Investigation of practical initial attenuation image estimates in TOF-MLAA reconstruction for PET/MR *Med. Phys.* **43** 4163–73

Cheng L, Ahn S, Shanbhag D, Qian H, Deller T and Wiesinger F 2016b Joint estimation of activity and attenuation: application to non-FDG TOF PET/MR clinical data *Proc. IEEE Nuclear Science Symp. Medical Imaging Conf.* (https://doi.org/10.1109/NSSMIC.2016.8069388)

Conti M 2011 Why is TOF PET reconstruction a more robust method in the presence of inconsistent data? *Phys. Med. Biol.* **56** 155–68

Davison H, ter Voert E E G W, de Galiza Barbosa F, Veit-Haibach P and Delso G 2015 Incorporation of time-of-flight information reduces metal artifacts in simultaneous positron emission tomography/magnetic resonance imaging: a simulation study *Invest. Radiol.* **50** 423–9

Defrise M, Rezaei A and Nuyts J 2012 Time-of-flight PET data determine the attenuation sinogram up to a constant *Phys. Med. Biol.* **57** 885–99
Edmund J M and Nyholm T 2017 A review of substitute CT generation for MRI-only radiation therapy *Radiat. Oncol.* **12** 28
Erdoğan H and Fessler J A 1999a Ordered subsets algorithms for transmission tomography *Phys. Med. Biol.* **44** 2835–51
Erdoğan H and Fessler J A 1999b Monotonic algorithms for transmission tomography *IEEE Trans. Med. Imaging* **18** 801–14
Fraum T J, Fowler K J and McConathy J 2015 PET/MRI: emerging clinical applications in oncology *Acad. Radiol.* **23** 220–36
Fuin N, Pedemonte S, Catalano O A, Izquierdo-Garcia D, Soricelli A, Salvatore M, Heberlein K, Hooker J M, Van Leemput K and Catana C 2017 PET/MRI in the presence of metal implants: completion of the attenuation map from PET emission data *J. Nucl. Med.* **58** 840–5
Grant F D, Fahey F H, Packard A B, Davis R T, Alavi A and Treves S T 2008 Skeletal PET with ^{18}F-fluoride: applying new technology to an old tracer *J. Nucl. Med.* **49** 68–78
Heiss W-D 2016 Hybrid PET/MR imaging in neurology: present applications and prospects for the future *J. Nucl. Med.* **57** 993–5
Heußer T, Rank C M, Berker Y, Freitag M T and Kachelrieß M 2017 MLAA-based attenuation correction of flexible hardware components in hybrid PET/MR imaging *EJNMMI Phys.* **4** 12
Heußer T, Rank C M, Freitag M T, Dimitrakopoulou-Strauss A, Schlemmer H-P, Beyer T and Kachelrieß M 2016 MR-consistent simultaneous reconstruction of attenuation and activity for non-TOF PET/MR *IEEE Trans. Nucl. Sci.* **63** 2443–51
Hofmann M, Pichler B and Schölkopf B and Beyer T 2009 Towards quantitative PET/MRI: a review of MR-based attenuation correction techniques *Eur. J. Nucl. Med. Mol. Imaging* **36** S93–104
Hofmann M, Steinke F, Scheel V, Charpiat G, Farquhar J, Aschoff P, Brady M, Schölkopf B and Pichler B J 2008 MRI-based attenuation correction for PET/MRI: a novel approach combining pattern recognition and atlas registration *J. Nucl. Med.* **49** 1875–83
Hofmann M *et al* 2001 Biokinetics and imaging with the somatostatin receptor PET radioligand ^{68}Ga-DOTATOC: preliminary data *Eur. J. Nucl. Med.* **28** 1751–7
Huang L-K and Wang M-J J 1995 Image thresholding by minimizing the measure of fuzziness *Pattern Recognit.* **28** 41–51
Hudson H M and Larkin R S 1994 Accelerated image reconstruction using ordered subsets of projection data *IEEE Trans. Med. Imaging* **13** 601–9
Hunter D R and Lange K 2012 A tutorial on MM algorithms *Am. Stat.* **58** 30–7
Keereman V, Fierens Y, Broux T, De Deene Y, Lonneux M and Vandenberghe S 2010 MRI-based attenuation correction for PET/MRI using ultrashort echo time sequences *J. Nucl. Med.* **51** 812–8
Keereman V, Mollet P, Berker Y, Schulz V and Vandenberghe S 2013 Challenges and current methods for attenuation correction in PET/MR *Magn. Reson. Mater. Phys.* **26** 81–98
Kinahan P E, Hasegawa B H and Beyer T 2003 X-ray-based attenuation correction for positron emission tomography/computed tomography scanners *Semin. Nucl. Med.* **33** 166–79
Laymon C M and Bowsher J E 2013 Anomaly detection and artifact recovery in PET attenuation correction images using the likelihood function *IEEE J. Sel. Top. Signal Process.* **7** 137–46
Laymon C M, Bowsher J E, Carney J P J and Blodgett T M 2006 Scatter correction requirements for likelihood-based attenuation artifact correction in PET *Proc. IEEE Nuclear Science Symp. Medical Imaging Conf.* vol 4 pp 2151–4
Laymon C M, Bowsher J E and Turkington T G 2003 Recovery of localized defects in PET attenuation-correction images *Proc. IEEE Nuclear Science Symp. Medical Imaging Conf.* vol 3 pp 1949–52
Levin C S, Maramraju S H, Khalighi M M, Deller T W, Delso G and Jansen F 2016 Design features and mutual compatibility studies of the time-of-flight PET capable GE SIGNA PET/MR system *IEEE Trans. Med. Imaging* **35** 1907–14
Leynes A P, Yang J, Shanbhag D D, Kaushik S S, Seo Y, Hope T A, Wiesinger F and Larson P E Z 2017 Hybrid ZTE/Dixon MR-based attenuation correction for quantitative uptake estimation of pelvic lesions in PET/MRI *Med. Phys.* **44** 902–13
Li H, El Fakhri G and Li Q 2013 Direct MAP estimation of attenuation sinogram using TOF PET data and anatomical information *Fully Three-Dimensional Image Reconstruction in Radiology and Nuclear Medicine Proc.* vol 3 pp 405–8
Li Q, Li H, Kim K and El Fakhri G 2017 Joint estimation of activity image and attenuation sinogram using time-of-flight positron emission tomography data consistency condition filtering *J. Med. Imaging* **4** 023502
Li Y, Defrise M, Metzler S D and Matej S 2015 Transmission-less attenuation estimation from time-of-flight PET histo-images using consistency equations *Phys. Med. Biol.* **60** 6563–83
Liao P-S, Chen T-S and Chung P-C 2001 A fast algorithm for multilevel thresholding *J. Inf. Sci. Eng.* **17** 713–27
Martinez-Möller A and Nekolla S G 2012 Attenuation correction for PET/MR: problems, novel approaches and practical solutions *Z. Med. Phys.* **22** 299–310
Martinez-Möller A, Souvatzoglou M, Delso G, Bundschuh R A, Chefd'hotel C, Ziegler S I, Navab N, Schwaiger M and Nekolla S G 2009 Tissue classification as a potential approach for attenuation correction in whole-body PET/MRI: evaluation with PET/CT data *J. Nucl. Med.* **50** 520–6
Mehranian A, Arabi H and Zaidi H 2016 Quantitative analysis of MRI-guided attenuation correction techniques in time-of-flight brain PET/MRI *Neuroimage* **130** 123–33
Mehranian A and Zaidi H 2015a Impact of time-of-flight PET on quantification errors in MR imaging-based attenuation correction *J. Nucl. Med.* **56** 635–41
Mehranian A and Zaidi H 2015b Clinical assessment of emission- and segmentation-based MR-guided attenuation correction in whole-body time-of-flight PET/MR imaging *J. Nucl. Med.* **56** 877–83
Mehranian A and Zaidi H 2015c Emission-based estimation of lung attenuation coefficients for attenuation correction in time-of-flight PET/MR *Phys. Med. Biol.* **60** 4813–33
Mehranian A and Zaidi H 2015d Joint estimation of activity and attenuation in whole-body TOF PET/MRI using constrained Gaussian mixture models *IEEE Trans. Med. Imaging* **34** 1808–21
Mihlin A and Levin C S 2017 An expectation maximization method for joint estimation of emission activity distribution and photon attenuation map in PET *IEEE Trans. Med. Imaging* **36** 214–24
Nekolla S G and Rischpler C 2016 Assessing myocardial metabolism with hybrid PET imaging: instrumentation, concepts, and workflows *Curr. Pharm. Des.* **22** 96–104
Nuyts J, Bal G, Kehren F, Fenchel M, Michel C and Watson C 2013 Completion of a truncated attenuation image from the attenuated PET emission data *IEEE Trans. Med. Imaging* **32** 237–46
Nuyts J, Dupont P, Stroobants S, Benninck R, Mortelmans L and Suetens P 1999 Simultaneous maximum *a posteriori* reconstruction of attenuation and activity distributions from emission sinograms *IEEE Trans. Med. Imaging* **18** 393–403
Otsu N 1979 A threshold selection method from gray-level histograms *IEEE Trans. Syst. Man Cyber.* **9** 62–6
Qian H, Manjeshwar R and Thielemans K 2010 A comparative study of multiple scatter estimations in 3D PET *Proc. IEEE Nuclear Science Symp. Medical Imaging Conf.* pp 2700–2

Rezaei A, Defrise M, Bal G, Michel C, Conti M, Watson C and Nuyts J 2012 Simultaneous reconstruction of activity and attenuation in time-of-flight PET *IEEE Trans. Med. Imaging* **31** 2224–33

Rezaei A, Defrise M and Nuyts J 2014 ML-reconstruction for TOF-PET with simultaneous estimation of the attenuation factors *IEEE Trans. Med. Imaging* **33** 1563–72

Rota Kops E and Herzog H 2007 Alternative methods for attenuation correction for PET images in MR-PET scanners *Proc. IEEE Nuclear Science Symp. Medical Imaging Conf.* vol 6 pp 4327–30

Salomon A, Goedicke A, Schweizer B, Aach T and Schulz V 2011 Simultaneous reconstruction of activity and attenuation for PET/MR *IEEE Trans. Med. Imaging* **30** 804–13

Salvo K and Defrise M 2017 sMLACF: a generalized expectation-maximization algorithm for TOF-PET to reconstruct the activity and attenuation simultaneously *Phys. Med. Biol.* **62** 8283–313

Samarin A, Hüllner M, Queiroz M A, Stolzmann P, Burger I A, von Schulthess G and Veit-Haibach P 2015 ^{18}F-FDG-PET/MR increases diagnostic confidence in detection of bone metastases compared with ^{18}F-FDG-PET/CT *Nucl. Med. Commun.* **36** 1165–73

Schneck J F 1996 The role of magnetic susceptibility in magnetic resonance imaging: MRI magnetic compatibility of the first and second kinds *Med. Phys.* **23** 815–50

Schramm G, Maus J, Hofheinz F, Petr J, Lougovski A, Beuthien-Baumann B, Platzek I and van den Hoff J 2014 Evaluation and automatic correction of metal-implant-induced artifacts in MR-based attenuation correction in whole-body PET/MR imaging *Phys. Med. Biol.* **59** 2713–26

Schulz V *et al* 2011 Automatic, three-segment, MR-based attenuation correction for whole-body PET/MR data *Eur. J. Nucl. Med. Mol. Imaging* **38** 138–52

Sekine T, ter Voert E E G W, Warnock G, Buck A, Huellner M W, Veit-Haibach P and Delso G 2016 Clinical evaluation of zero-echo-time attenuation correction for brain ^{18}F-FDG-PET/MRI: Comparison with atlas attenuation correction *J. Nucl. Med.* **57** 1927–32

Shanbhag D D, Kaushik S S, Thiruvenkadam S, Wiesinger F, Ahn S, Mullick R and Manjeshwar R M 2015 MR driven PET-attenuation correction in presence of metal implants using anatomy context driven decisioning *Int. Society for Magnetic Resonance in Medicine (ISMRM) Annual Meeting*

Surti S and Karp J S 2015 Advances in time-of-flight PET *Phys. Med.* **32** 12–22

Tai Y F and Piccini P 2004 Applications of positron emission tomography (PET) in neurology *J. Neurol. Neurosurg. Phychiatry* **75** 669–76

ter Voert E E G W, Veit-Haibach P, Ahn S, Wiesinger F, Khalighi M M, Levin C S, Iagaru A H, Zaharchuk G, Huellner M and Delso G 2017 Clinical evaluation of TOF versus non-TOF on PET artifacts in simultaneous PET/MR: a dual center experience *Eur. J. Nucl. Med. Mol. Imaging* **44** 1223–33

Tustison N J, Avants B B, Cook P A, Zheng Y, Egan A, Yushkevich P A and Gee J C 2010 N4ITK: improved N3 bias correction *IEEE Trans. Med. Imaging* **29** 1310–20

Vandenberghe S and Marsden P K 2015 PET-MRI: a review of challenges and solutions in the development of integrated multimodality imaging *Phys. Med. Biol.* **60** R115–54

Vandenberghe S, Mikhaylova E, D'Hoe E, Mollet P and Karp J S 2016 Recent developments in time-of-flight PET *EJNMMI Phys.* **3** 3

Wahl R L, Jacene H, Kasamon Y and Lodge M A 2009 From RECIST to PERCIST: evolving considerations for PET response criteria in solid tumors *J. Nucl. Med.* **50** 122S–50S

Wang G, Catana C and Qi J 2012 Joint reconstruction of attenuation and emission images from PET data using MR-derived attenuation prior *IEEE Nuclear Science Symp. Medical Imaging Conf.*

Watson C C 2000 New, faster, image-based scatter correction for 3D PET *IEEE Trans. Nucl. Sci.* **47** 1587–94

Wiesinger F *et al* 2018 Zero TE-based pseudo-CT image conversion in the head and its application in PET/MR attenuation correction and MR-guided radiation therapy planning *Magn. Reson. Med.* accepted (https://doi.org/10.1002/mrm.27134)

Wiesinger F, Sacolick L I, Menini A, Kaushik S S, Ahn S, Veit-Haibach P, Delso G and Shanbhag D D 2016 Zero TE MR bone imaging in the head *Magn. Reson. Med.* **75** 107–14

Wollenweber S D, Ambwani S, Delso G, Lonn A H R, Mullick R, Wiesinger F, Piti Z, Tari A, Novak G and Fidrich M 2013a Evaluation of an atlas-based PET head attenuation correction using PET/CT and MR patient data *IEEE Trans. Nucl. Sci.* **60** 3383–90

Wollenweber S D, Ambwani S, Lonn A H R, Shanbhag D D, Thiruvenkadam S, Kaushik S, Mullick R, Qian H, Delso G and Wiesinger F 2013b Comparison of 4-class and continuous fat/water methods for whole-body, MR-based PET attenuation correction *IEEE Trans. Nucl. Sci.* **60** 3391–8